Fundamenta Informaticae 146 (2016) 219–230
DOI 10.3233/FI-2016-1383
IOS Press

An Orientation-space Super Sampling Technique for Six-dimensional Diffraction Contrast Tomography

Nicola Viganò*
MATEIS, INSA Lyon, CNRS (UMR5510), Univ. Lyon, F-69621 Lyon, France, and
ESRF, The European Synchrotron, F-38043 Grenoble, France
nicola.vigano@esrf.fr

Kees Joost Batenburg*
CWI, Amsterdam, 1098 XG Amsterdam, The Netherlands, and
University of Leiden, Mathematical Institute, 2300 RA Leiden, The Netherlands

Wolfgang Ludwig
MATEIS, INSA Lyon, CNRS (UMR5510), Univ. Lyon, F-69621 Lyon, France, and
ESRF, The European Synchrotron, F-38043 Grenoble, France

Abstract. Diffraction contrast tomography (DCT) is an X-ray full-field imaging technique that allows for the non-destructive three-dimensional investigation of polycrystalline materials and the determination of the physical and morphological properties of their crystallographic domains, called grains. This task is considered more and more challenging with the increasing intra-granular deformation, also known as orientation-spread. The recent introduction of a six-dimensional reconstruction framework in DCT (6D-DCT) has proven to be able to address the intra-granular crystal orientation for moderately deformed materials.
The approach used in 6D-DCT, which is an extended sampling of the six-dimensional combined position-orientation space, has a linear scaling between the number of sampled orientations, which determine the orientation-space resolution of the problem, and computer memory usage. As a result, the reconstruction of more deformed materials is limited by their high resource requirements from a memory and computational point of view, which can easily become too demanding for the currently available computer technologies.
In this article we propose a super-sampling method for the orientation-space representation of the six-dimensional DCT framework that enables the reconstruction of more deformed cases by reducing the impact on system memory, at the expense of longer reconstruction times. The use of super-sampling can further improve the quality and accuracy of the reconstructions, especially in cases where memory restrictions force us to adapt to inadequate (undersampled) orientation-space sampling.

*Also works: University of Antwerp, iMinds-Vision Lab, B-2610 Antwerp, Belgium.
Address for correspondence: MATEIS, INSA Lyon, CNRS (UMR5510), Université de Lyon, F-69621 Lyon, France.

Received July 2016; revised July 2016.

1. Introduction

X-rays, through the use of computed tomography (CT), allow for non-destructive three-dimensional investigation of materials' inner structure and properties. X-ray diffraction in particular probes the crystallographic properties of the analysed objects.

Diffraction contrast tomography (DCT), is an extended-beam near-field technique in the domain of three-dimensional X-ray microscopy. Thanks to the illumination of extended three-dimensional regions in the analysed objects, DCT allows for fast measurements, and so, it also allows to follow the time evolution of crystalline materials, with high spatial resolution.

The original focus of DCT was of the reconstruction of the grain shape and orientation in undeformed or nearly-undeformed materials. With the advent of [1], which proposes a six-dimensional formulation of the DCT reconstruction problem (6D-DCT), and the following work based on the said six-dimensional model [2, 3], the focus has been shifted more and more towards the sub-grain orientation determination in moderately deformed materials. Especially in [2], where 6D-DCT was proven to be able to retrieve the local orientation of large textured regions, also the limits of this approach were exposed.

The six-dimensional model is based on a discrete sampling of both the real-space, and the orientation-space occupied by a given grain, which suffers from the so called "curse of dimensionality", where the increased number of dimensions in a sampling problem, increases the associated memory requirements in an exponential way. The reconstruction of large real-space regions, exhibiting moderate to high orientation-spreads, implicates that large amounts of memory are needed for the computer algorithms to reconstruct these regions.

While the real-space resolution in a DCT reconstruction is linked to the acquisition resolution, the orientation-space resolution is determined by the size of the orientation-space bounding box, where we expect to find all the possible orientations present in the to-be-reconstructed region, and the number of sampled points. Moderate to high deformations imply larger orientation-space bounding boxes, where to sample orientations. As a consequence, for constant resolution, one would need considerably more orientations, than for lower levels of deformation, but memory is limited and at some point we have to make a compromise and increase the sampling interval (i.e. decrease the ultimate resolution).

In this article we present a super-sampling framework in the orientation-space to alleviate the shortcomings linked to these memory constrained problems, and possibly to allow for the reconstruction of extreme cases which were previously considered impossible to solve with nowadays computer technology.

2. Method

We are now going to introduce the diffraction geometry used in DCT, then we will describe how this translates to its projection model and finally we will discuss the super-sampling extension of this model.

2.1. Diffraction geometry

The usual setup of diffraction contrast tomography, when using a monochromatic beam, consists of a rotation stage where the sample is positioned, and an high resolution imaging detector positioned immediately behind the sample.

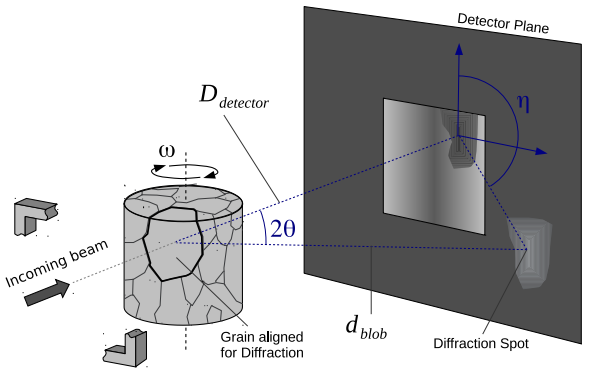

Figure 1: Diffraction geometry of a DCT experiment.

As the sample rotates by angle ω, it gives rise to diffracted beams each time the Bragg condition is met for one of the grains. Some of those diffracted beams will intersect the detector, and give rise to diffraction spots, which, in the absence of intra-granular orientation spread, correspond to 2D projections of the 3D grain volume. After diffraction spot segmentation and indexation based on Friedel pairs (hkl and $\bar{h}\bar{k}\bar{l}$ reflections of the same grain observed for ω_0 and $\omega_0 + 180°$) the 3D grain structure can be reconstructed by means of iterative tomographic reconstruction techniques. The reader interested in details concerning the setup, acquisition procedures and initial processing steps like segmentation, Friedel pair matching and indexation of near-field X-ray diffraction data is referred to [4] and [5].

In the presence of non-negligible intra-granular orientation spread, the parallel projection assumption used in conventional (three-dimensional) DCT gets violated. Each of the sub-orientations present in a grain is associated to a slightly different projection geometry and the diffraction signal associated to a given Bragg reflection is observed as a distorted, three-dimensional diffraction volume, which then takes the name of diffraction "blob". It is parametrized by two spatial coordinates u and v (detector pixel coordinates) and a rotation angle ω (image number). An alternative parametrization of the blob coordinates, instead of the triplet (ω, u, v), is given by the triplet (ω, θ, η), where the angle θ is the aperture angle typical of an hkl-family, and η is the angle between the (u, v) position of the blob on the detector and the projection of the rotation axis on the detector, having the projected center of the diffracting grain as vertex (fig. 1).

2.2. Projection model in Diffraction Contrast Tomography

As previously introduced in [1], the single grain reconstruction problem can be cast as the solution of an underdetermined linear system:

$$\boldsymbol{A}\mathbf{x} = \mathbf{b} \tag{1}$$

where $\mathbf{x}$ is the volume to be reconstructed, $\mathbf{b}$ represents the images recorded on the detector, and $\boldsymbol{A}$ is the so called projection matrix, which embodies the projection geometry of the tomographic problem.

If the reconstruction takes the local orientations in the voxels into account, it will be set in a six-dimensional space, given by the outer product of the real-space and the orientation-space defined as:

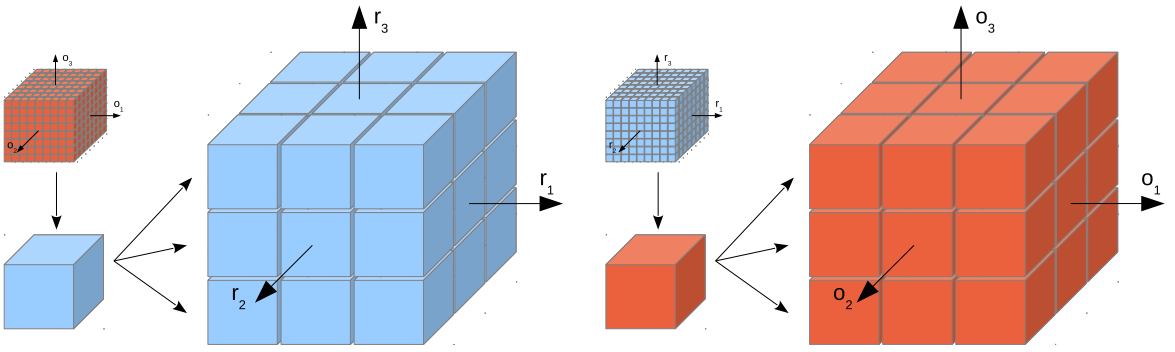

(a) Orientation-space in real-space voxels (b) Real-space orientation-space in voxels

Figure 2: Comparison among the two different interpretations of a six-dimensional space that combines orientation and position information.

$\mathbb{X}^6 = \mathbb{R}^3 \otimes \mathbb{O}^3$. In this representation, the gray level values associated to each six-dimensional voxel are the scattering intensities for the given orientation $\mathbf{r} \in \mathbb{O}^3$ at the real-space position $\mathbf{x} \in \mathbb{R}^3$ of the sample. To model the orientation-space we chose to use the Rodrigues parametrization [6, 7].

The introduction of the orientation-space components in the projection model can be easily done in two equivalent ways: (a) a collection of orientation distribution functions (ODFs) for each of the real-space voxels (figure 2a), (b) using a regular grid sampling of the three-dimensional orientation-space, and associating a real-space volume to each of them (figure 2b). While the first representation is the more intuitive for the materials scientist, the second is the more computationally efficient. We will now focus on case (b) which is the one chosen for the 6D-DCT.

The actual implementation of case (b) will assume that for each sampled point in orientation-space, we will associate a real-space volume, which has the exact same size for each of the sampled orientations. We will also assume that the sampled points will be the center of the orientation-space voxels. The resulting volume memory requirements will be given by the simple formula:

$$N\text{bytes} = p_x p_y p_z n_x n_y n_z \times (\text{bytes per voxel}) \tag{2}$$

where n_x, n_y and n_z will respectively be the number of sampled points along the x, y and z axes of the real-space, and p_x, p_y and p_z will respectively be the number sampled points along the x, y and z axes of the orientation-space.

Finally, in this context, equation (1) can be recast as the composition of the following pieces:

$$\begin{pmatrix} \boldsymbol{A}_{11} & \cdots & \boldsymbol{A}_{1P} \\ \vdots & \ddots & \vdots \\ \boldsymbol{A}_{M1} & \cdots & \boldsymbol{A}_{MP} \end{pmatrix} \begin{pmatrix} \mathbf{x}_1 \\ \vdots \\ \mathbf{x}_P \end{pmatrix} = \begin{pmatrix} \mathbf{b}_1 \\ \vdots \\ \mathbf{b}_M \end{pmatrix} \tag{3}$$

where each volume $\mathbf{x}_i$, which has a fixed orientation, would contribute to each diffraction blob $\mathbf{b}_j$ on the detector, with $i = 1, \ldots, P$, $j = 1, \ldots, M$, P the total number of sampled orientations and M the total number of measured diffraction blobs.

2.3. Super-sampled projection model

As the projection matrix model is based on a discrete sampling of the six-dimensional space formed by the outer product of a three-dimensional real-space and a three-dimensional orientation space, the resolution in the sampling grid will play an important role for determining the accuracy of the tomographic model itself. As mentioned earlier, the real-space sampling resolution is given by the detector pixel size, which translates into the real-space voxel size. The orientation-space resolution instead is not fixed by the experiment alone, but also depends on material characteristics. This means that in memory constrained cases, where large orientation-space bounding boxes are used, in conjunction with having to deal with large regions in real-space, also a considerable number of orientations will be needed.

From equation (2), it follows that for an increase of resolution of a factor 2 in orientation-space, the memory requirements would become $2^3 = 8$ times larger. For a constant number N of elements in $\underline{x}$, this implies that for growing orientation-space bounding boxes, associated with large real-space bounding boxes, a lower orientation-space resolution could be expected. As a consequence, this would lead to the distance among the sampled points to grow, and to the assumption of one single chosen orientation to approximate the whole associated orientation-space voxel to fail.

In real-space, a strip model of the projection rays could help with moderate inhomogeneity of the voxel size compared to the detector pixel sizes, especially when the pixels are larger than the voxels, because the strips would intercept all the voxels having an overlap with the strip. In this case, instead, Joseph's method wouldn't be able to associate some voxels to the related detector pixels, but various oversampling techniques exist to solve this problem, like the super-sampling method used in [8] for their super-resolution application.

Since in orientation-space each point determines a projection geometry in real-space, it is not obvious how to model a projection geometry corresponding to the integral of a three-dimensional interval of orientations.

It is in fact easier to start from the back-projection super-sampling technique presented in [8], that is based on a sampling approach, and model a similar type of orientation super-sampling.

The orientation space voxels, as shown in the inset of figure (3), instead of being represented by a single sampled point in the center of the orientation space volume forming the said voxel, they could be divided into $S = s^3$ sub-voxels, that would forward and back project the same associated real-space volume, but with slightly different orientations given by the centers of the new sub-voxels and projection coefficients of $1/S$ instead of 1. The new projection matrix would then look like:

$$\boldsymbol{A}\mathbf{x} = \sum_{i}^{P} \sum_{j}^{S} \frac{1}{S} \boldsymbol{A}_{ij} \mathbf{x}_i = \mathbf{b} \tag{4}$$

where for a given volume i, the sub-matrices $\boldsymbol{A}_i = \{\boldsymbol{A}_{i1}, \boldsymbol{A}_{i2}, \ \ldots, \boldsymbol{A}_{iS}\}$ are the associated orientation-space sub-voxel sampled orientations.

For memory constrained configurations, the use of this type of super-sampling can alleviate considerably artifacts due to otherwise poor sampling. In fact, it increases by a factor s the coverage of the orientation-space, resulting in $S = s^3$ times finer sampling. On the other hand, this doesn't translate in an effective increase in orientation-space resolution by a factor s, for which we would then need to use SP volumes, instead of the P volumes used in this configuration.

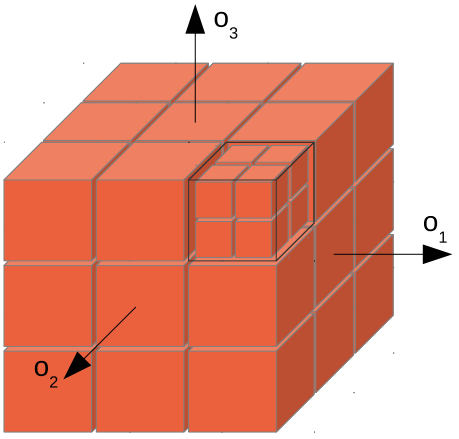

Figure 3: Orientation space super sampling, as shown by the top right front voxel of the sampled grid. While the usual sampling would pick the center of the voxels associated to the volumes like in figure 2b, in this case we instead pick the centers of the sub-voxels and associate all of them with the same real-space volume.

2.4. Reconstruction algorithm

The reconstruction algorithm is the same that was used in [2], and it is based on a recast of equation (1) into a minimization problem, where the solution of the algorithm is the vector that minimizes the following functional:

$$\mathbf{x}^* = \underset{\mathbf{x}}{\operatorname{argmin}} ||\boldsymbol{A}\mathbf{x} - \mathbf{b}||_2 + \lambda || \left(|\nabla S\mathbf{x}|\right) ||_1 \tag{5a}$$

$$\text{subject to: } \mathbf{x} \geq \mathbf{0} \tag{5b}$$

where S is the operator that sums all the components in orientation-space for each real-space voxel, and the l_1-norm over the absolute value of the gradient is the total variation operator $\mathrm{TV}(\cdot)$ [9, 10]. More precisely, the operator S is defined as the projection $S : \mathbb{X}^6 = \mathbb{R}^3 \otimes \mathbb{O}^3 \rightarrow \mathbb{R}^3$ from the six-dimensional space $\mathbb{X}^6$ to the three-dimensional real-space $\mathbb{R}^3$. In fact, if we sum all the contributions from the orientation-space to each position in real-space, we obtain a pure positional three-dimensional volume that contains the information about the shape of the reconstructed grain.

As a result, thanks to the addition of the $\mathrm{TV}(\cdot)$ operator, the algorithm resolving the minimization problem expressed in equation (5), minimizes the projection distance from the detector images, and promotes the grain boundary sharpness and the grey level homogeneity inside the grain at the same time.

For the solution of the functional in equation (5) we used the same algorithmic instance proposed in [1].

2.5. Hardware and software implementation details

The reconstructions were performed on a desktop machine with two Intel® Xeon® CPUs E5-2630 working at 2.30GHz, an NVIDIA® GeForce GTX 980 GPU card and 64GB of RAM. The soft-

ware was implemented in Matlab[1] and C++, using the ASTRA Toolbox[2] for the projection and back-projection of the volumes.

3. Results and discussion

To verify the model established in the previous section, we decided to use highly deformed three-dimensional synthetic dataset, which is based on the one used in [1]. The new dataset instance is still based on a $50 \times 50 \times 50$ voxels volume, where the deformation pattern has been rescaled, from an orientation spread of $1\ degree$ to $5\ degree$s across the volume.

While using the same phantom, we decided to perform two different tests at two different orientation-space sampling resolutions, to test the behaviour of the super-sampling framework in two different scenarios: (a) poor orientation-space resolution, to see if this extension was able to mitigate the problem due to a bad coverage of orientation-space, (b) decent but not optimal orientation-space resolution, to see if the proposed framework would still be able to push the reconstruction towards better results.

The $3.32 \times 3.10 \times 3.27\ degree$s orientation-space bounding box is sampled using $8 \times 7 \times 8$ and $18 \times 16 \times 17$ sampling points respectively.

We then compared the shapes of the reconstructed objects and the orientation-space accuracy of the reconstruction with and without various parameters s of super-sampling. In all the reconstructions 60 blobs were used.

3.1. Orientation-space resolution

Before entering the discussion about the results we would like to briefly discuss the maximum expected resolution for this type of diffraction experiments in orientation-space, and how to compute the actual resolution in the reconstructed region of interest.

As it happens for the position-space, where the maximum resolution in the one determined by the detector pixel size, for the orientation-space, the maximum achievable resolution will also be determined by the experimental conditions, but with a slightly higher degree of complexity.

The parallelism between the two spaces is even more obvious if we think that for a fixed position in orientation-space, a point (ω, u, v) on the detector defines a projection line in real-space, and for a fixed point in real-space, a position (ω, θ, η) on the detector defines a line in orientation-space [11, 12]. This means that the maximum resolution on the detector for (ω, θ, η) will define the maximum resolution in orientation-space.

Since the z-axis is aligned with the sample rotation axis, the experimental integration stepping of the ω angle will directly translate into the resolution along the z-axis of the orientation-space. This means that:

$$r_{z,\max} = \delta\omega \tag{6}$$

where $r_{z,\max}$ stands for maximum resolution along the z-axis and $\delta\omega$ is the experimental ω integration step.

For what concerns the x-axis and the y-axis the resolution will be related to the minimum detectable angle in η, which in turn depends on several factors, including the distance of the detector from the

[1]Registered trademark of *MathWorks*

[2]https://github.com/astra-toolbox

sample, the hkl-family of each blob, and the effective size of the detector pixels. If we define the effective detector pixel size as:

$$\Delta\text{pixel} = |\cos(\eta_0)|\Delta u + |\sin(\eta_0)|\Delta v \tag{7}$$

where Δu and Δv are the pixel edge sizes in the u and v directions respectively, and η_0 is the average η of the considered blob, we can compute the maximum achievable resolution along the *x*-axis and the *y*-axis as the following:

$$r_{x,y,\text{max}} = \delta\eta = \tan^{-1}\left(\frac{\Delta\text{pixel}}{d_{\text{blob}}}\right) = \tan^{-1}\left(\frac{\Delta\text{pixel}}{D_{\text{detector}}\tan(2\theta)}\right) \tag{8}$$

where d_{blob} is the distance between the centroid of the blob and the projection of the grain center on the detector, and D_{detector} is the distance between the grain and the detector (fig. 1).

So, by taking a $\delta\omega = 0.1\ degree$s, $d_{\text{detector}} = 6\ mm$, a maximum $\theta = 5.73\ degree$s, an associated $\eta = 42\ degree$s and $\Delta u = \Delta v = 1\ \mu m$, we have that the maximum achievable resolutions in orientation-space will be:

$$r_{z,\text{max}} = 0.1\ degrees \tag{9a}$$

$$r_{x,y,\text{max}} = \tan^{-1}\left(\frac{1\mu m}{6\times10^3\mu m\times\tan(2\times5.73\ degrees)}\right) = 0.067\ degrees \tag{9b}$$

Finally, if we compute the orientation-space sampling resolution r in one direction d as:

$$r_d = \frac{l_d}{(p_d - 1)} \tag{10}$$

where l_d is the size of the bounding box and p_d is number of sampling points in that specific direction, we obtain resolutions of $0.47\times0.51\times0.46\ degree$s and $0.19\times0.20\times0.20\ degree$s, respectively for the two test cases, which are well above the smallest achievable precisions, from the experimental conditions.

On the other hand, to reach the maximum allowed resolution in orientation-space, we would need a grid of $34\times47\times49$ sampling points for the example in this article. With a real-space volume composed by $72\times72\times72$ single precision floating point voxels, according to equation (2), we would need almost 110GB of RAM to store the six-dimensional representation of the reconstruction space. Since the algorithm needs two copies for each of those volumes, the total requirements will be 220GB of RAM, making this relatively small test case quite challenging for the currently available workstations.

3.2. Low resolution reconstructions

We here analyse the results from the (a) scenario, which had a memory occupation of only 638 MBs for the volumes used, leading to a $\sim$ 2 GBs total memory occupation.

The regular reconstruction took 530s $\simeq$ 9min, in comparison with the super-sampled reconstruction that took 2707s $\simeq$ 45m with a super-sampling factor $s = 2$, and 7793s $\simeq$ 2h10min with a super-sampling factor $s = 3$.

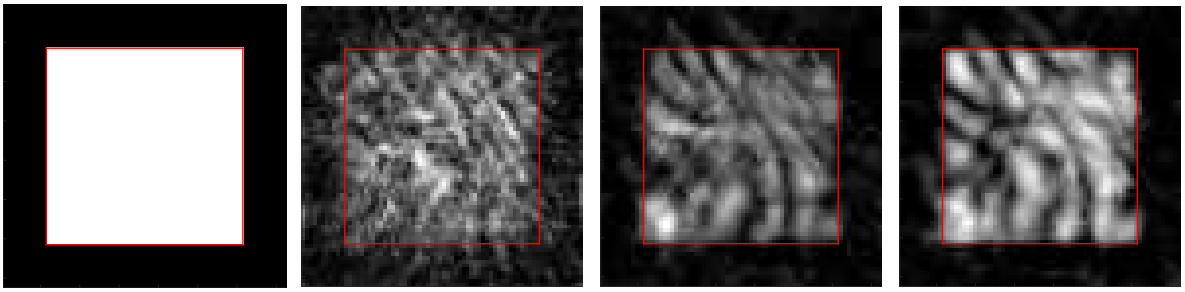

(a) Phantom (b) Normal reconstruction (c) Super-sampling $s = 2$ (d) Super-sampling $s = 3$

Figure 4: Comparison of the shape retrieved by the reconstructions for a $8 \times 7 \times 8$ sampling points grid, in the normal and super-sampled case with super-sampling factors $s = 2$ and $s = 3$.

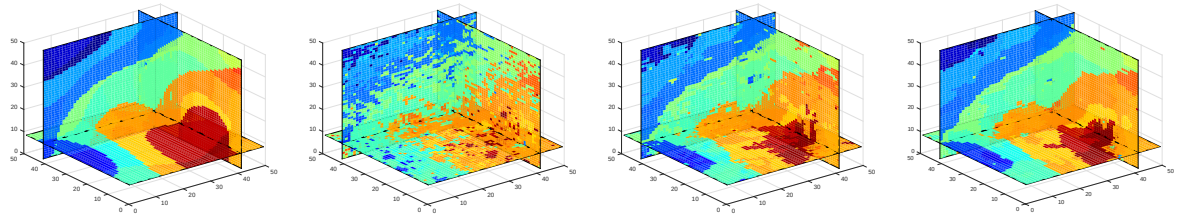

(a) Phantom (b) Normal reconstruction (c) Super-sampling $s = 2$ (d) Super-sampling $s = 3$

Figure 5: Comparison of the orientation-space morphology reconstructed with a sampling of $8 \times 7 \times 8$ grid points, in the normal and super-sampled case with super-sampling factors $s = 2$ and $s = 3$.

As it can be seen in figure (4b), the chosen resolution is not sufficient to reconstruct the shape of the cubic grain used in this synthetic test case. From figure (4c) instead we see that a small oversampling factor of $s = 2$ already improves the reconstruction of the selected slice, even if the orientation-space coverage is still not enough to achieve a decent result. Figure (4d) suggests that a bigger super-sampling factor of $s = 3$ might help to further alleviate the shortcomings of a bad orientation-space sampling resolution, for what concerns the shape and homogeneity of the reconstructed object.

In figure (5), a different aspect is taken into account: we look at the orientation-space reconstruction accuracy for the different reconstruction parameters. In this figure, we use the orientation coloring used in [1], to visualize orientation domains in an easily recognizable way for the human eye, where each color is associated with a region in the sample orientation-space, and where contiguous regions have similar colors.

Again, as noted for the shape of the reconstructed object, an oversampling factor $s = 2$ (figure 5c), and $s = 3$ (figure 5d), give a visible improvement over the reconstructions without any oversampling, which is in line with the expectations from figure (4b).

3.3. Moderate resolution reconstructions

In the higher resolution case (b), which needed 6.8 GBs for the volumes, leading to a $\sim$ 15 GBs total memory occupation, the regular reconstruction took 5679s $\simeq$ 1h34min, in comparison with the super-sampled reconstruction that took 26947s $\simeq$ 7h29min, with super-sampling parameter $s = 2$.

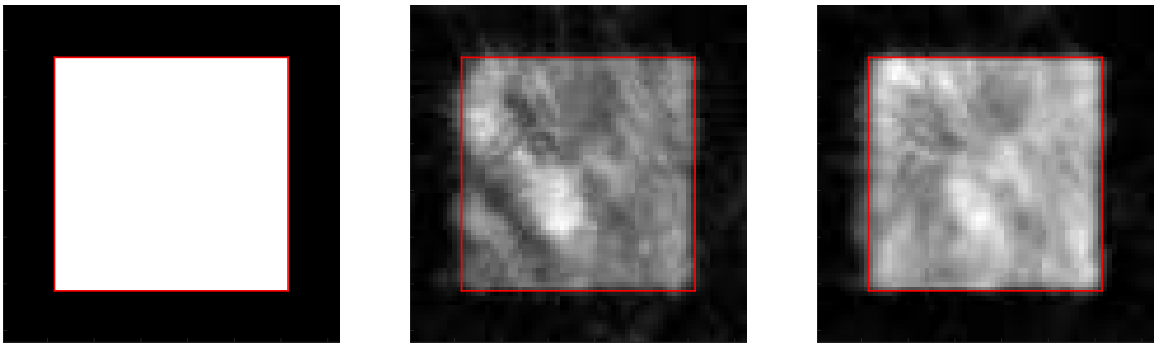

(a) Phantom (b) Normal reconstruction (c) Super-sampling reconstruction

Figure 6: Comparison of the shape retrieved by the reconstructions for a $18 \times 16 \times 17$ sampling points grid, in the normal and super-sampled case with a super-sampling factor $s = 2$.

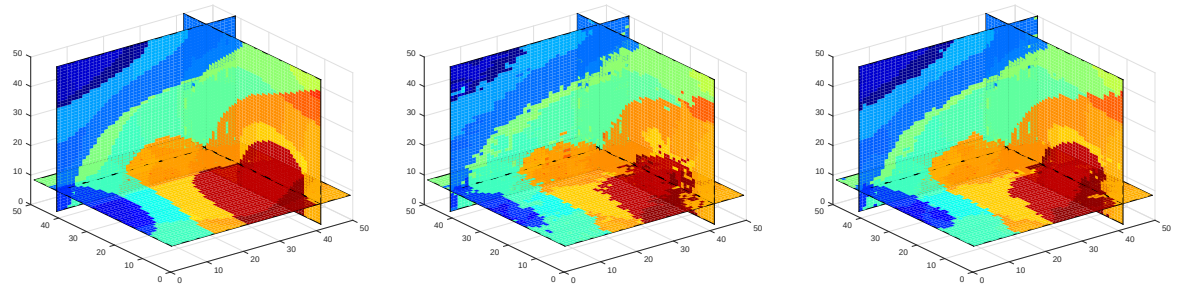

(a) Phantom (b) Normal reconstruction (c) Super-sampling reconstruction

Figure 7: Comparison of the orientation-space morphology reconstructed with a sampling of $18 \times 16 \times 17$ grid points, in the normal and super-sampled case with a super-sampling factor $s = 2$.

In this scenario, the higher super-sampling values like $s = 3$ from the previous case were not tested, due to higher needs in term of computational power and the moderate advantage in terms of reconstruction quality.

As expected, figure (6) as compared to figure (4), shows that by increasing the orientation-space resolution, even without any super-sampling, the algorithm already gives a better reconstruction for this test case. However, the quality of the reconstruction can be further enhanced by introducing the oversampling with a factor of $s = 2$. In fact, figure (6c) shows a clearly smoother and space filling reconstruction than figure (6b).

We observe the same behavior in figure (7), where especially the interfaces among the different orientation domains were resolved with higher precision in the super-sampled reconstruction.

4. Conclusions and outlook

As shown in the previous section, in both study cases, the proposed super-sampling method provided better results both in terms of grain shape reconstruction quality and local orientation determination accuracy.

The biggest improvement obtained thanks to this super-sampling technique was obviously in the low resolution case study, where the non super-sampled reconstruction (figures 4b and 5b) showed extremely poor reconstruction quality. In fact, the super-sampled reconstruction gave visible improvements both in the reconstruction of the shape, and in the determination of the local orientation (figures 4c and 5c), without however being able to outperform the higher resolution reconstruction of the second test case.

In spite of the fact that higher orientation-space super-sampling parameters s can significantly improve the orientation-space representation of the chosen sampling, it cannot actually increase the orientation-space resolution. This means that it has no influence on the formula in equation (10), and that it is not possible to achieve a better result using the coarse sampling of $8 \times 7 \times 8$ with super-sampling parameter $s = 2$ or $s = 3$, instead of the non-supersampled $18 \times 16 \times 17$ grid. By comparing figure (4d) with figure (6b) and figure (5d) with figure (7b), the results indeed confirm that the orientation-space super-sampling cannot fix a bad orientation-space sampling. Moreover, the computational cost of higher super-sampling parameters s, can become prohibitive for bigger reconstruction problems.

In conclusion we see this super-sampling technique as a good tool for allowing to retrieve useful information from memory limited cases, where the size of the real-space volumes, and the available memory, do limit the quality of coverage of the orientation-space. The longer computation times are paid off by the increased accuracy of the projector, and as a consequence, of the increased quality of the reconstructions.

In the future, in addition to this orientation-space super-sampling technique, also other strategies could be incorporated to enable the analysis of more difficult and interesting scientific scenarios. For instance, if we allow for a small decrease in real-space resolution, we could imagine the combined use of this orientation-space super-sampling with a real-space super-sampling acting on binned real-space volumes. The real-space super-sampling would balance the real-space voxels' increased size, while at the same time allowing for an increased orientation-space resolution, at constant memory consumption.

As a final remark, since the biggest cost center in the reconstruction resides in the forward-projection and back-projection of the real-space volumes, it is reasonable to assume that in the future, when newer and more powerful graphics chipsets will be available, the computation times could be greatly reduced. In addition, the projection of each volume is independent of the projection of every other volume, except for a small part of the calculation. This means that it is also possible to run multiple volume projections at the same time if multiple GPUs are available. As a result, with modern multi-GPUs solutions and the use of the ASTRA library, the reconstruction speed could already be at least doubled, with minimal changes in the code.

Acknowledgments

NV and WL acknowledge financial support of the French National Research Agency (ANR), project: ANR 2010 BLAN 0935, and the German Research Foundation (DFG), priority programme: SPP 1466.

KJB acknowledges financial support of the Netherlands Organization for Scientific Research (NWO), project nr. 639.072.005.

The authors acknowledge COST Action MP1207 for networking support.

NV would like to thank Willem Jan Palenstijn for the precious discussions.

References

[1] Viganò N, Ludwig W, Batenburg KJ. Reconstruction of local orientation in grains using a discrete representation of orientation space. Journal of Applied Crystallography. 2014 oct;47(6):1826–1840. doi:10.1107/S1600576714020147.

[2] Viganò N, Tanguy A, Hallais S, Dimanov A, Bornert M, Batenburg KJ, et al. Three-dimensional full-field X-ray orientation microscopy. Scientific Reports. 2016 feb;6. Available from: http://www.nature.com/articles/srep20618. doi:10.1038/srep20618.

[3] Viganò N, Nervo L, Valzania L, Singh G, Preuss M, Batenburg KJ, et al. A feasibility study of full-field X-ray orientation microscopy at the onset of deformation twinning. Journal of Applied Crystallography. 2016 apr;49(2). doi:10.1107/S1600576716002302.

[4] Ludwig W, Reischig P, King A, Herbig M, Lauridsen EM, Johnson G, et al. Three-dimensional grain mapping by x-ray diffraction contrast tomography and the use of Friedel pairs in diffraction data analysis. The Review of scientific instruments. 2009 mar;80(3):033905. doi:10.1063/1.3100200.

[5] Reischig P, King A, Nervo L, Viganó N, Guilhem Y, Palenstijn WJ, et al. Advances in X-ray diffraction contrast tomography: flexibility in the setup geometry and application to multiphase materials. Journal of Applied Crystallography. 2013 mar;46(2):297–311. doi:10.1107/S0021889813002604.

[6] Frank FC. Orientation mapping. Metallurgical Transactions A. 1988;19(3):403–408. doi:10.1007/BF02649253.

[7] Kumar A, Dawson PR. Computational modeling of f.c.c. deformation textures over Rodrigues' space. Acta Materialia. 2000 jun;48(10):2719–2736. doi:10.1016/S1359-6454(00)00044-6.

[8] Van Aarle W, Batenburg KJ, Van Gompel G, Van de Casteele E, Sijbers J. Super-resolution for computed tomography based on discrete tomography. IEEE transactions on image processing : a publication of the IEEE Signal Processing Society. 2014;23(3):1181–93. doi:10.1109/TIP.2013.2297025.

[9] Candes E, Romberg J. l1-magic: Recovery of sparse signals via convex programming. 2005; p. 1–19. http://statwebstanfordedu/~candes/l1magic/.

[10] Sidky EY, Jørgensen JH, Pan X. Convex optimization problem prototyping for image reconstruction in computed tomography with the Chambolle-Pock algorithm. Physics in medicine and biology. 2012 may;57(10):3065–91. doi:10.1088/0031-9155/57/10/3065.

[11] Morawiec A, Field D. Rodrigues parameterization for orientation and misorientation distributions. Philosophical Magazine A. 1996;73:1113–1130. doi:10.1080/01418619608243708.

[12] Poulsen HF. Three-Dimensional X-Ray Diffraction Microscopy. vol. 205 of Springer Tracts in Modern Physics. Berlin, Heidelberg: Springer Berlin Heidelberg; 2004. doi:10.1007/b97884.